

**NOAA NESDIS  
CENTER for SATELLITE APPLICATIONS and  
RESEARCH**

**ALGORITHM THEORETICAL BASIS DOCUMENT**

**ABI Earth Radiation Budget -  
Downward Longwave Radiation: Surface  
(DLR)**

*Hai-Tien Lee<sup>(1)</sup>, Istvan Laszlo<sup>(2)</sup> and Arnold Gruber<sup>(1)</sup>*

<sup>(1)</sup>CICS/ESSIC-NOAA/UMCP

<sup>(2)</sup>NOAA/NESDIS/STAR, AOSC/UMCP

Version 2.0  
September 24, 2010

## TABLE OF CONTENTS

1	INTRODUCTION .....	10
1.1	Purpose of This Document.....	10
1.2	Who Should Use This Document .....	10
1.3	Inside Each Section.....	10
1.4	Related Documents .....	10
1.5	Revision History .....	11
2	OBSERVING SYSTEM OVERVIEW.....	11
2.1	Product Generated.....	11
2.2	Instrument Characteristics .....	11
3	ALGORITHM DESCRIPTION.....	14
3.1	Algorithm Overview .....	14
3.2	Processing Outline .....	15
3.3	Algorithm Input .....	15
3.3.1	Primary Sensor Data .....	15
3.3.2	Ancillary Data .....	16
3.3.2.1	Static Data.....	16
3.3.2.2	Derived Data.....	16
3.4	Theoretical Description.....	17
3.4.1	Physics of the Problem.....	17
3.4.2	Mathematical Description.....	18
3.4.3	Algorithm Output.....	22
3.4.3.1	Output .....	22
3.4.3.2	Quality Flags.....	22
3.4.3.3	Metadata .....	23
3.4.3.4	Diagnostic Output.....	24
4	TEST DATA SETS AND OUTPUTS .....	24
4.1	Simulated/Proxy Input Data Sets.....	24
4.2	Output from Simulated/Proxy Inputs Data Sets.....	25
4.2.1	Accuracy and Precisions of Estimates .....	34
4.2.2	Error Budget.....	34
5	PRACTICAL CONSIDERATIONS.....	35
5.1	Numerical Computation Considerations.....	35
5.2	Programming and Procedural Considerations .....	35
5.3	Quality Assessment and Diagnostics .....	35
5.4	Exception Handling .....	36
5.5	Algorithm Validation .....	36
6	ASSUMPTIONS AND LIMITATIONS .....	36
6.1	Performance .....	36
6.1.1	Graceful Degradation.....	36
6.2	Assumed Sensor Performance .....	37
6.3	Pre-Planned Product Improvements .....	37
6.3.1	Improvement 1 .....	37
6.3.2	Improvement 2 .....	37
6.3.3	Improvement 3 .....	37

6.3.4 Improvement 4 .....	37
7 REFERENCES .....	37
Appendix 1: Common Ancillary Data Sets .....	39
1. MDS_L2_TPW_5KM_FILE .....	39
a. <i>Data description</i> .....	39
b. <i>Interpolation description</i> .....	39
2. NWP_GFS .....	39
a. <i>Data description</i> .....	39
b. <i>Interpolation description</i> .....	40

## LIST OF FIGURES

Figure 3-1 High Level Flowchart of the ABI DLR algorithm illustrating the main processing sections.....	15
Figure 3-2 Surface temperature adjustment in response to the application of lapse rate threshold, shown as a function of local time. The lapse rate threshold resulted in nearly 30°K of reduction in surface temperature around the local noon that in part reduced the over-estimation of the noontime DLR. ....	20
Figure 3-3 DLR adjustment in response to the application of lapse rate threshold, shown as a function of local time. The lapse rate threshold resulted in up to about 10 Wm <sup>-2</sup> of reduction in DLR around the local noon that in part reduced the over-estimation of the noontime DLR. ....	21
Figure 3-4 Original (i.e., without lapse rate threshold) DLR estimation errors plotted as a function of the DLR adjustment amount by applying the lapse rate threshold. The application of lapse rate threshold reduces the DLR overestimation errors by about 20% to 50%, depending on the site and atmospheric conditions. ....	22
Figure 4-1 Examples of the coverage of GOES Sounding retrievals (blue) related to the ground stations (red) in SURFRAD and ARM networks. Although the GOES Sounders make observations at every 30 minutes interval, the sounding product is only available by hourly. ....	25
Figure 4-2 Comparison of GOES Sounder-based DLR estimates against SURFRAD observations for homogeneous clear sky scenes.....	26
Figure 4-3 DLR errors are shown as a function of the surface net LW where the low net LW values are usually associated with the presence of low clouds. ....	27
Figure 4-4 Examples of the time series of SURFRAD flux measurements and GOES DLR estimates. LPLA DLR (orange diamond); PIR downwelling thermal radiation (white curve); PIR upwelling thermal radiation (yellow curve); PSP downwelling solar radiation, values scaled by one tenth (cyan curve). The typical .....	28
Figure 4-5 Satellite DLR estimation errors are shown as functions of the local time. The DLR estimation seems to have local time-dependent biases when compared to the SURFRAD ground observations.....	29
Figure 4-6 Difference of the precipitable water between GOES retrieval and RAOB. GOES total precipitable water for the seven SURFRAD sites has a mean 0.11 cm bias compared to the RAOB. Except with slightly larger degree of spread during later afternoon hours, the PW differences do not seem to have diurnal dependence that could explain the DLR errors.....	29
Figure 4-7 DLR differences between satellite retrievals and ground observations are plotted as a function of the standard deviation of the satellite clear sky DLR retrievals within 0.5° radius of the ground stations. The linear fit shows a negative slope, indicating the effects of scene in-homogeneity on the estimation biases. ....	30
Figure 4-8 Examples of DLR errors in relation with surface temperature retrieval errors in clear sky condition. The red triangle symbol indicate the surface air temperature observed in the 10 m tower at the station, while the green dot indicates the satellite retrieved surface temperature. (Note that the pressure levels of the two symbols can be	

different that is the error in the surface pressure analysis the satellite retrieval used) A significant portion of the DLR errors can be attributed to the surface temperature errors in these scenarios (see stats at the bottom left corner in each plot). .....	31
Figure 4-9 Comparison of satellite retrieved DLR versus the ground observations. The satellite DLR retrievals use the 10-m air temperature to represent the surface temperature. It is clearly shown that these DLR retrievals are much more accurate than those using satellite-retrieved surface temperatures. ....	31
Figure 4-10 Using the 10m air temperature as the surface temperature input for DLR retrieval nearly entirely removed the diurnal dependence of errors that were previously seen. This strongly suggests that the GOES skin temperature retrieval (as part of the Sounding product) has diurnally dependent errors. ....	32
Figure 4-11 This plot suggests that the DLR errors seem to be dependent on the total precipitable water. ....	32
Figure 4-12 Comparison of satellite retrieved DLR versus the ground observations. The satellite DLR retrievals use the 10-m air temperature and RAOB profiles. ....	33
Figure 4-13 DLR errors are shown to be strongly dependent on the total precipitable water, with a correlation of 0.32. This is consistent with the previous experiment that only uses in-situ surface temperature. This seems to suggest representativeness errors in the LPLA algorithm effective emissivity parameterization that we need to pursue further investigations. ....	34

## LIST OF TABLES

Table 2-1. ABI channel numbers and wavelengths relevant to the ABI DLR retrieval. . .	13
Table 2-2. F&PS requirements for the ABI DLR product.....	14
Table 3-1. ABI primary sensor input data used by the DLR algorithm.....	16
Table 3-2. Regression coefficients.....	16
Table 3-3. Temperature profile, total precipitable water, surface pressure and surface temperature. ....	17
Table 4-1 DLR comparison statistics. Note that the apparent cloud contaminated cases were eliminated with the empirical filtering on the surface Net LW fluxes.....	26
Table 4-2 Error statistics for comparisons between CERES-retrieved and ground measured surface downward LW fluxes.....	26
Table 4-3 F&PS requirement and the estimated DLR accuracy and precisions.....	34

## LIST OF ACRONYMS

ABI	Advanced Baseline Imager
ASTER	Advanced Space-borne Thermal Emission and Reflection Radiometer
ATBD	Algorithm Theoretical Basis Document
AWG	Algorithm Working Group
CERES	The Cloud and the Earth's Radiant Energy System
COVE	CERES Ocean Validation Experiment\
CRTM	Community Radiative Transfer Model
DLR	Downward Longwave Radiation at Surface
DLW	Downward Longwave Radiation at Surface
GFS	Global Forecast Model
GSIP	GOES Surface Insolation Product
JHU	Johns Hopkins University
LST	Land skin temperature
PIR	Eppley Precision Infrared Radiometer
SST	Sea surface temperature
SURFRAD	NOAA Surface Radiation Budget Network
ULR	Upward Longwave Radiation at Surface
ULW	Upward Longwave Radiation at Surface

## ABSTRACT

This Algorithm Theoretical Basis Document (ATBD) describes the physical and mathematical basis of the algorithm developed to retrieve the ***Downward Longwave Radiation: Surface (DLR)*** by the Advanced Baseline Imager (ABI) onboard the geostationary satellite GOES-R. The DLR algorithm is derived from the ABI-retrieved temperature profile, total column precipitable water, and surface temperature. The DLR retrieval is performed for clear-sky condition due to the unavailability of the cloud base information from ABI cloud retrieval. Algorithm evaluation was conducted with various proxy data and ground truth observations. It is shown that this algorithm could meet the F&PS requirements.

## 1 INTRODUCTION

The downward longwave radiation at the surface is the total downward thermal radiative flux density emitted and reflected by the atmosphere that reaches the earth's surface. It is one of the four radiative flux components that determine the radiation budget at the earth's surface. The other three radiative fluxes are the upward longwave radiation, the incoming solar radiation (insolation), and the reflected solar radiation.

### 1.1 Purpose of This Document

The Earth Radiation Budget (ERB) Downward Longwave Radiation: Surface (DLR) algorithm theoretical basis document (ATBD) provides a high level description of and the physical basis of the algorithm developed by the Radiation Budget Application Team (AT) of the GOES-R Algorithm Working Group (AWG) for the estimation of DLR at the earth's surface. The ATBD provides the observing system overview, algorithm description, explanation of test data sets and outputs, practical considerations for implementation, assumptions and limitations for the performance assessment, and references.

### 1.2 Who Should Use This Document

The intended users of this document are those interested in understanding the physical basis of the algorithms and the error characteristics of this product. This document also provides information useful to anyone maintaining or modifying the original algorithm.

### 1.3 Inside Each Section

This document is broken down into the following main sections.

- **System Overview:** Provides relevant details of the ABI and provides a brief description of the product generated by the algorithm.
- **Algorithm Description:** Provides all the detailed description of the algorithm including its physical basis, its input and output.
- **Assumptions and Limitations:** Provides an overview of the current limitations of the approach and gives the plan for overcoming these limitations with further algorithm development.
- **Validation:** Provides summaries of up to date validation results and descriptions of error characteristics.

### 1.4 Related Documents

This document relates to the references given throughout and to the GOES-R Mission Requirements Document (MRD), and the GOES-R Ground Segment Functional and Performance Specification Document (F&PS).

## **1.5 Revision History**

Version 0.1 (Aug. 15, 2008)

The Version 0.1 ATBD draft accompanies the delivery of the Version 1 algorithm code package to the GOES-R AWG Algorithm Integration Team (AIT).

Version 1.0 (Sep. 26, 2009)

Version 1.0 describes the algorithm at the 80% F&PS requirement level, and accompanies the delivery of the Version 4 algorithm code package to the GOES-R AWG Algorithm Integration Team (AIT).

Version 2.0 (Sep. 5, 2010)

Version 2.0 describes the algorithm at the 100% F&PS requirement level, and accompanies the delivery of the Version 5 algorithm code package to the GOES-R AWG Algorithm Integration Team (AIT). Newly implemented features include the lapse rate threshold and the graceful degradation for surface temperature input. This revision also includes the definitions of metadata, quality flags, and diagnostic output.

## **2 OBSERVING SYSTEM OVERVIEW**

This section provides an overview of the retrieval strategy, the algorithm, and the input needed. It also describes the products generated by the algorithm and the requirements it places on the sensor.

### **2.1 Product Generated**

The algorithm generates a single product, the Downward Longwave Radiation at Surface (DLR) product. DLR is the total downward thermal radiative flux density arriving the earth surface from the atmosphere above it whereas most of this radiation is emitted by the atmosphere, primarily by gases and clouds. There is also a very small contribution from the surface in the form of the fraction of upward surface emission that is reflected back to the surface by the overlaying atmosphere. In the DLR retrieval algorithm, the reflection component is neglected. DLR is given in the units of watts per square meter.

DLR strongly depends on the moisture and temperature profiles of the atmosphere. Since these profiles will only be available for clear-sky pixels from ABI, retrieval of DLR from the current algorithm will not be performed for cloudy pixels. Calculation of DLR will also be limited to slant path observations to within the local zenith angle limit of the sounding retrievals.

### **2.2 Instrument Characteristics**

The final channel set used for retrieval is still being determined as the algorithm is further developed and validated. Table 2-1 summarizes the ABI channels relevant for DLR retrieval. The ABI DLR F&PS requirements are listed in Table 2-2.

Table 2-1. ABI channel numbers and wavelengths relevant to the ABI DLR retrieval.

<i>Channel ID</i>	<i>Wavelength Microns</i>	<i>Hor. Res.</i>	<i>Upper and lower 50% response points (in microns)</i>	<i>Noise @ Ref.</i>	<i>Max. Level</i>	<i>Used for DLR</i>
1	0.47	1km	0.45±0.01 - 0.49±0.01	300/1	100 %	
2	0.64	0.5km	0.59±0.01 - 0.69±0.01	300/1	100 %	
3	0.865	1km	0.8455±0.01 - 0.8845±0.01	300/1	100 %	
4	1.378	2km	1.3705±0.005 - 1.3855±0.005	300/1	100 %	
5	1.61	1km	1.58±0.01 - 1.64±0.01	300/1	100 %	
6	2.25	2km	2.225±0.01 - 2.275±0.01	300/1	100 %	
7	3.90	2km	3.80±0.05 - 4.00±0.05	0.1 K	400 K	
8	6.185	2km	5.77±0.03 - 6.6±0.03	0.1 K	300 K	✓
9	6.95	2km	6.75±0.03 - 7.15±0.03	0.1 K	300 K	✓
10	7.34	2km	7.24±0.02 - 7.44±0.02	0.1 K	320 K	✓
11	8.5	2km	8.3±0.03 - 8.7±0.03	0.1 K	330 K	✓
12	9.61	2km	9.42±0.02 - 9.8±0.03	0.1 K	300 K	✓
13	10.35	2km	10.1±0.1 - 10.6±0.1	0.1 K	330 K	✓
14	11.2	2km	10.8±0.1 - 11.6±0.1	0.1 K	330 K	✓
15	12.3	2km	11.8±0.1 - 12.8±0.1	0.1 K	330 K	✓
16	13.3	2km	13.0±0.06 - 13.6±0.06	0.3 K	305 K	✓

Table 2-2. F&amp;PS requirements for the ABI DLR product.

Name	User & Priority	Geographic Coverage (G, H, C, M)	Vertical Resolution	Horizontal Resolution	Mapping Accuracy	Measurement Range	Measurement Accuracy	Refresh Rate/Coverage Time	Refresh Rate Option (Mode 4)	VAGL
Downward Longwave Radiation: Surface	GOES-R	C	N/A	25 km	5 km	50-750 W/m <sup>2</sup>	25 W/m <sup>2</sup> for known cloud fraction	60 min	5 min	3238 sec
Downward Longwave Radiation: Surface	GOES-R	FD	N/A	25 km	4 km	50-750 W/m <sup>2</sup>	25 W/m <sup>2</sup> for known cloud fraction	60 min	5 min	806 sec

Product Measurement Precision	Temporal Coverage Qualifiers	Product Extent Qualifier	Cloud Cover Conditions Qualifier	Product Statistics Qualifier
20 W/m <sup>2</sup> for known cloud fraction	Day and Night	Quantitative out to at least 70 degrees LZA	N/A	Over specified geographic area
20 W/m <sup>2</sup> for known cloud fraction	Day and Night	Quantitative out to at least 70 degrees LZA	N/A	Over specified geographic area

### 3 ALGORITHM DESCRIPTION

#### 3.1 Algorithm Overview

The surface downward longwave radiation (DLR) is derived by a physical-statistical method using inputs from satellite retrievals. During the development, two algorithms were tested: the University of Maryland Cooperative Institute for Climate Studies (CICS) algorithm (Lee and Ellingson, 2002) and the NASA Langley Parameterized Longwave Algorithm (LPLA) (Gupta, 1989).

After careful evaluation and testing of both algorithms, the LPLA algorithm has been selected as the ABI DLR retrieval algorithm.

### 3.2 Processing Outline

The processing outline of the DLR is summarized in the Figure 3-1. This processing scheme is applied to each pixel.

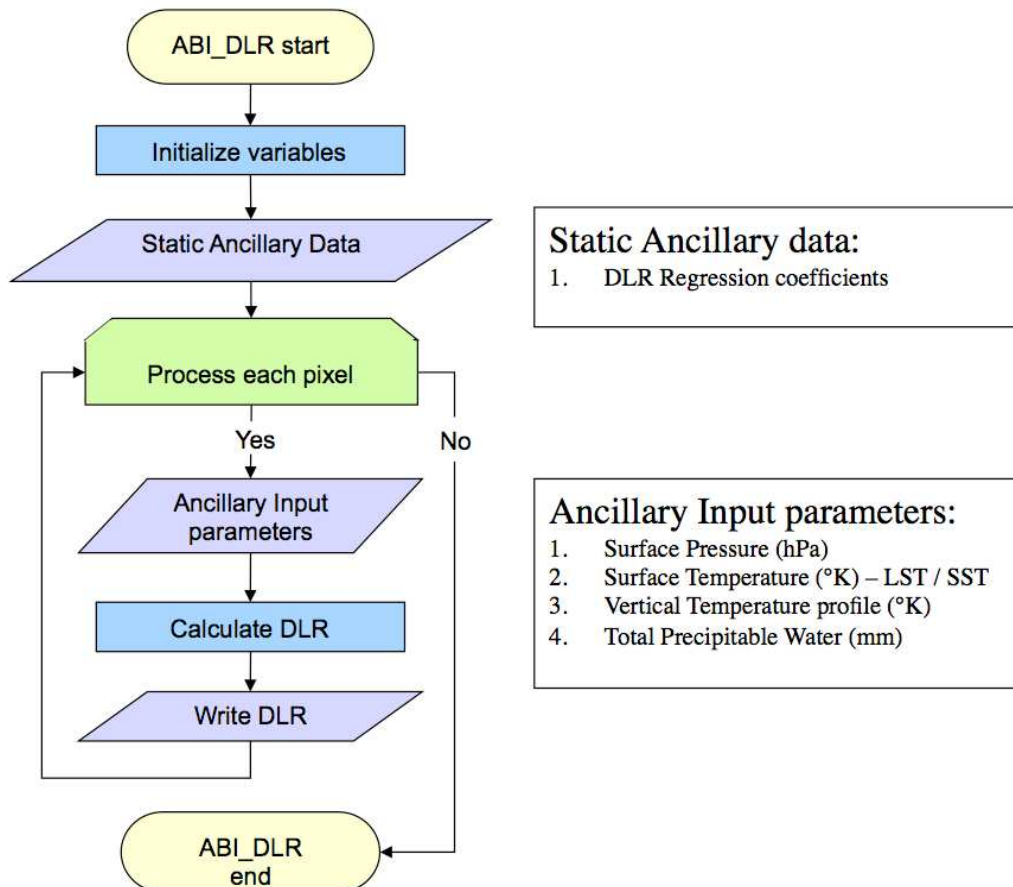


Figure 3-1 High Level Flowchart of the ABI DLR algorithm illustrating the main processing sections.

### 3.3 Algorithm Input

This section describes the input needed to process the DLR. The DLR derivation is for each pixel independent of the surrounding pixels.

#### 3.3.1 Primary Sensor Data

By primary sensor data, we mean information that is derived solely from the ABI observations and geolocation information.

The DLR algorithm does not require ABI radiance data. Other level 1b data used are listed in Table 3-1.

Table 3-1. ABI primary sensor input data used by the DLR algorithm.

Name	Type	Description	Dimension
Latitude	input	Center latitude	grid (xsize, ysize)
Longitude	input	Center longitude	grid (xsize, ysize)
View geometry	input	ABI local zenith angle	grid (xsize, ysize)
QC flags	input	ABI quality control flags with level 1b data	grid (xsize, ysize)

\* Grid (xsize and ysize) are the output grid dimension that is product specific and is determined by the post processing.

### 3.3.2 Ancillary Data

The algorithm uses two types of ancillary data:

- Static Non-ABI Data: regression coefficients (Table 3-2)
- ABI Derived Data: Temperature profiles, total precipitable water, surface pressure, surface temperature (Table 3-3)

#### 3.3.2.1 Static Data

The static data are the regression coefficients needed to calculate DLR (Table 3-2).

Table 3-2. Regression coefficients.

Name	Type	Description	Dimension
Regression Coefficients	input	ABI DLR regression coefficients	Floating number: 7

#### 3.3.2.2 Derived Data

Derived data includes vertical profile of temperature, total column precipitable water, surface temperature, and surface pressure (Table 3-3).

Table 3-3. Temperature profile, total precipitable water, surface pressure and surface temperature.

Name	Type	Description	Dimension
Temperature Profile	input	ABI retrieved Temperature profile	Floating number Array no. of sounding levels
Total Precipitable Water	input	ABI retrieved total precipitable water	Floating number
Surface Pressure	input	ABI retrieved surface pressure	Floating number
Surface Temperature	input	ABI retrieved surface temperature	Floating number

### 3.4 Theoretical Description

The downward longwave radiation (DLR) reaching the surface is the result of the atmospheric thermal emission and reflection. The reflection component is negligibly small because the scattering of thermal radiation is very weak in the atmosphere that most radiation is governed by the absorption/emission and transmission. The radiative transferring of the DLR is determined by the vertical distribution of the molecules, their optical properties, and temperature structure. Among gas form molecules, water vapor, due to its optical property and variability, is the most important as it accounts for a significant part of the clear sky DLR variation. For clear sky, the vertical distribution of the atmospheric temperature weighted by the distribution of the molecular optical transmissivity determines an effective atmospheric emitting temperature that can be applied to the Stefan-Boltzmann law to estimate the DLR.

#### 3.4.1 Physics of the Problem

The DLR is related to the downward specific intensity  $I_\nu(z=0, -\mu)$  at the earth's surface in an axial-symmetric atmosphere as

$$DLR = 2\pi \int_{LW} \int_0^1 I_\nu(z=0, -\mu) \mu d\mu d\nu \quad (3.4)$$

where  $\mu \equiv \cos(\theta)$ ,  $\theta$  is the local zenith angle, and  $\nu$  is the wave number or frequency that is integrated through the longwave spectrum, typically in wave number 0 to 3000  $\text{cm}^{-1}$ .

For clear sky condition, the specific intensity  $I_{\nu,0}(z=0;-\mu)$  that reaches the surface coming off a local zenith angle  $\theta$  from a plane parallel, horizontally homogeneous and non-scattering atmosphere in local thermal equilibrium can be expressed as,

$$I_{\nu,0}(z=0;-\mu) = -\int_0^{z_t} B_\nu(z') \frac{\partial \mathfrak{S}_\nu(0,z';-\mu)}{\partial z'} dz' \quad (3.5)$$

where  $B_\nu(z')$  is the Planck function evaluated at wave number  $\nu$  with the temperature at level  $z'$ , and  $\mathfrak{S}_\nu$  is the monochromatic transmittance.  $Z_t$  denotes the top of the atmosphere.

The parameterization of the atmospheric downward emission in the LPLA DLR algorithm is explained below. Details of the temperature and moisture profile retrievals are in the Soundings ATBD. For consistency, the skin temperature will be taken from the Sounding product.

### 3.4.2 Mathematical Description

The monochromatic downward longwave flux from a clear sky can be expressed as

$$F_{\nu,0}^\downarrow = -\int_0^{z_t} \pi B_\nu(z') \frac{\partial \mathfrak{S}_{F\nu}(0,z')}{\partial z'} dz' \quad (3.6)$$

where  $\mathfrak{S}_{F\nu}(0,z') \equiv 2 \int_0^1 \mathfrak{S}_\nu(0,z';-\mu) \mu d\mu$  is the monochromatic flux transmittance of the atmosphere.

One can always find a mean emission  $\bar{B}_\nu$  such that

$$F_{\nu,0}^\downarrow = \pi \bar{B}_\nu (1 - \mathfrak{S}_{F\nu}^{(0,z_t)}) \quad (3.7)$$

$(1 - \mathfrak{S}_{F\nu}^{(0,z_t)})$  is the monochromatic flux emittance of the atmosphere, assuming the reflectivity is negligible. The mean emission is defined by

$$\pi \bar{B}_\nu \equiv \frac{-\int_0^{z_t} \pi B_\nu(z') \frac{\partial \mathfrak{S}_{F\nu}(0,z')}{\partial z'} dz'}{(1 - \mathfrak{S}_{F\nu}^{(0,z_t)})} \quad (3.8)$$

Integrating the monochromatic flux over the full spectrum produces the total flux, DLR:

$$DLR = \int F_{\nu,0}^\downarrow d\nu = \int \pi \bar{B}_\nu (1 - \mathfrak{S}_{F\nu}^{(0,z_t)}) d\nu \quad (3.9)$$

One can always find an effective temperature  $T_{eff}$  with a corresponding effective emissivity  $\epsilon_{eff}$  such that

$$\sigma T_{eff}^4 = \int \pi B_\nu(T_{eff}) d\nu \equiv \int \pi \bar{B}_\nu d\nu \quad (3.10)$$

and,

$$\epsilon_{eff} \equiv \frac{\int \pi \bar{B}_v (1 - \mathfrak{S}_{F_v}^{(0, z_i)}) dv}{\int \pi \bar{B}_v dv} \quad (3.11)$$

where  $\sigma$  is the Stefan-Boltzmann constant.

Therefore, DLR is now equivalent to a grey body emission characterized by the effective emitting temperature  $T_{eff}$  and an effective atmospheric emissivity  $\epsilon_{eff}$ :

$$DLR = \epsilon_{eff} \cdot \sigma T_{eff}^4 \quad (3.12)$$

The LPLA DLR algorithm formulation follows the Stefan-Boltzmann law for a grey body in that it estimates the effective atmospheric emissivity and the effective emitting temperature. The LPLA deviates slightly from the Stefan-Boltzmann law in that the emission temperature is raised to the power 3.7 instead of 4. The regression coefficients were determined using data sets derived from radiative transfer model calculations with given collections of sounding samples.

The variation of this brightness temperature reflects the variation in the low tropospheric temperature structure that is modulated by the distribution and amount of water vapor. The atmosphere is assumed to be a grey body with an effective emissivity that corresponds to the defined effective emitting temperature. This effective emissivity is governed by the distribution and amount of water vapor, especially in the lower troposphere. The effective emissivity is parameterized as a function of the total precipitable water as a proxy to account for the overall water vapor modulation effects.

The LPLA clear sky DLR algorithm defines the effective atmospheric emitting temperature as the weighted average of surface temperature and the temperatures of the two lowest atmospheric layers (150 hPa of thickness). It writes,

$$DLR_{clr} = (A_0 + A_1 V + A_2 V^2 + A_3 V^3) \cdot T_e^{3.7} \quad (3.12)$$

$$T_e \equiv k_s T_s + k_1 T_1 + k_2 T_2 \quad (3.13)$$

where  $V \equiv \ln(PW)$

$DLR_{clr}$  – clear-sky surface downward longwave radiative flux density ( $Wm^{-2}$ )

$T_e$  – Effective emitting temperature ( $^{\circ}K$ )

$T_s$  = Surface Temperature ( $^{\circ}K$ )

$T_1$  = Layer 1 (Sfc-850hPa) Temperature ( $^{\circ}K$ )

$T_2$  = Layer 2 (850-700hPa) Temperature ( $^{\circ}K$ )

PW – total column precipitable water (mm-atm)

$k_i$ 's and  $A_i$ 's – regression coefficients

The regression coefficients currently used are:

$A_0=1.791e-7$ ,  $A_1=2.093e-8$ ,  $A_2=-2.748e-9$ ,  $A_3=1.184e-9$

$W_s=0.5$ ,  $W_1=0.4$ ,  $W_2=0.1$

The emissivity term is parameterized as a 3<sup>rd</sup> order polynomial function of total precipitable water. The Stefan-Boltzmann law was slightly modified in the way that the emitting temperature is raised by a power of 3.7 instead of 4 as this minimizes regression errors. The radiation data sets used in the regression analysis were simulated with the radiative transfer model developed by Darnell et al (1983).

The detailed description of the LPLA DLR algorithm can be found in Gupta, 1989.

### Algorithm Modifications

During the validation studies, we found that the use of skin temperature to define the effective emitting temperature could cause biases under certain conditions that mostly related to strong discontinuity between the skin and surface air temperatures. A new procedure was devised to correct this problem.

Gupta et al. (2010) devised a lapse rate threshold for the lowest layer to 10°K/100hPa. This reduces the overestimation of DLR for superheated surface conditions. The performance assessment is basically unchanged – the standard deviation of DLR differences is slightly improved from 12.5 Wm<sup>-2</sup> to 12.2 Wm<sup>-2</sup>. Figures 3-2, 3-3, and 3-4 show the effects and the improvement of applying this procedure to the DLR retrieval.

In ABI DLR implementation, we defines the lowest layer as the layer between surface and the lowest sounding level that is at least 25 hPa away from the surface pressure. This guaranties that the lapse rate test is applied to a layer at least 25 hPa thick.

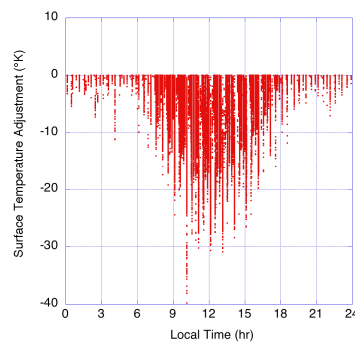


Figure 3-2 Surface temperature adjustment in response to the application of lapse rate threshold, shown as a function of local time. The lapse rate threshold resulted in nearly 30°K of reduction in surface temperature around the local noon that in part reduced the over-estimation of the noontime DLR.

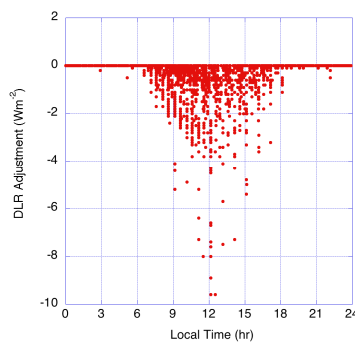


Figure 3-3 DLR adjustment in response to the application of lapse rate threshold, shown as a function of local time. The lapse rate threshold resulted in up to about  $10 \text{ Wm}^{-2}$  of reduction in DLR around the local noon that in part reduced the over-estimation of the noontime DLR.

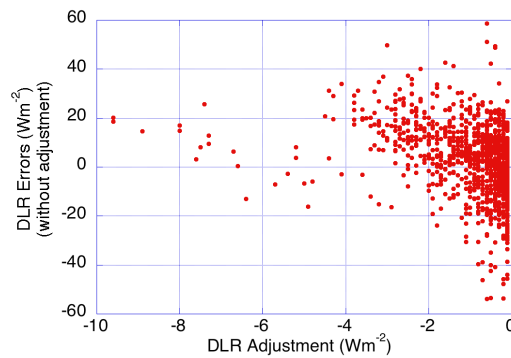


Figure 3-4 Original (i.e., without lapse rate threshold) DLR estimation errors plotted as a function of the DLR adjustment amount by applying the lapse rate threshold. The application of lapse rate threshold reduces the DLR overestimation errors by about 20% to 50%, depending on the site and atmospheric conditions.

### 3.4.3 Algorithm Output

#### 3.4.3.1 Output

The algorithm output is the downward longwave radiative flux density at the earth's surface with the unit of  $\text{Wm}^{-2}$ . The ABI DLR retrieval is performed on the pixel level. These pixel values are averaged into the specified horizontal resolution at the product packaging stage. To be consistent with the horizontal resolution of the radiation products, the DLR good quality values are averaged within the required spatial grids (latitude and longitude rectangular grid). The spatial resolution of these grids is such that they accommodate the horizontal spatial resolution requirements listed in Table 2-2 with the assumption that one degree in latitude and longitude space equals 100 km. To meet the 60 minute Mode 3 refresh requirement, the DLR product only needs to be run once every hour.

#### 3.4.3.2 Quality Flags

- For ABI DLR algorithm, the QC flags are three two-byte integers:
  - QC\_INPUT: 16-bit integer containing input and degradation quality flags
  - QC\_RET: 16-bit integer containing retrieval quality flags
- The bit values are defined to start from the least significant bit.
- The QC Flags are diagnostic output on the 5x5 pixels basis (following sounding unit target definition)

#### QC\_INPUT: Input

Bit	Quality Flag Name	Meaning	
		zero (default)	one
0	QC_INPUT_SOUND	Valid temperature sounding product input	Invalid temperature sounding profiles (QC flag check)
1	QC_INPUT_TPW	Valid TPW product input	Invalid TPW product (QC flag check)
2	QC_INPUT_LST	Valid LST input	Invalid LST (QC flag check)
3	QC_INPUT_SST	Valid SST input	Invalid SST (QC flag check)
4	QC_INPUT_PS	Valid surface pressure input	Invalid surface pressure (range check)
5	QC_INPUT_TSFC	Valid satellite surface temp-	Both LST and SST are invalid

		erature retrieval (LST or SST) is available	
6	QC_INPUT_TAIR	Surface temperature is obtained from LST or SST	Extrapolated surface air temperature is used
7			
8			
9			
10			
11			
12			
13			
14			
15			

### QC\_RET: Success/failure of retrieval

Bit	Quality Flag Name	Meaning	
		zero (default)	one
0	QC_RET_OVERALL	Overall success of retrieval	Overall failure of retrieval
1	QC_RET_INPUT	Valid input parameters	Retrieval failed due to invalid input
2	QC_RET_OUTPUT	Valid DLR output	Retrieval failed due to invalid DLR output (out of range)
3	QC_RET_LRATE	Lapse rate threshold is not exceeded	Lapse rate threshold exceeded. Adjustment of surface temperature is performed.
4			
5			
6			
7			

### 3.4.3.3 Metadata

These Metadata provide quick tracking of product properties over the respective domains. They are derived for each hourly map.

#### Conus Product

Name	Description	Data Type	
META_DLR_CN_MEAN	Mean DLR over Conus domain	Real*4	
META_DLR_CN_STD	Standard deviation of DLR over Conus	Real*4	
META_DLR_CN_MAX	Maximum DLR over Conus	Real*4	
META_DLR_CN_MIN	Minimum DLR over Conus	Real*4	
META_DLR_CN_VALID	Percentage of DLR with each QA flag value	Real*4	

#### Full Disc Product

Name	Description	Data Type	
META_DLR_FD_MEAN	Mean DLR over FD domain	Real*4	
META_DLR_FD_STD	Standard deviation of DLR over FD	Real*4	
META_DLR_FD_MAX	Maximum DLR over FD	Real*4	
META_DLR_FD_MIN	Minimum DLR over FD	Real*4	
META_DLR_FD_VALID	Percentage of DLR with each QA flag	Real*4	

	value		
--	-------	--	--

### 3.4.3.4 Diagnostic Output

The parameters defined here are the diagnostic output that will be generated for product validation and verification purposes.

For each of the output grid boxes at the product output resolution:

Name	Description	Data Type	Dimension
NUM_DLR_RET	Number of successful DLR retrievals at pixel level	Integer*2	grid (xsize, ysize)
STD_DLR_RET	Standard deviation of DLR retrievals	Real*4	grid (xsize, ysize)

\* Grid (xsize and ysize) are the output grid dimension that is product specific and is determined by the post processing.

## 4 TEST DATA SETS AND OUTPUTS

### 4.1 Simulated/Proxy Input Data Sets

The ABI candidate DLR algorithm was evaluated primarily using the GOES Sounder sounding retrievals collocated with the Eppley Precision Infrared Radiometer (PIR) observations from SURFRAD networks. The GOES Sounder sounding retrievals are theoretically better than the future ABI algorithms because ABI lacks sufficient number of CO<sub>2</sub> channels.

The GOES Sounding product was used as the primary surrogate data source to evaluate the surface DLR algorithms. This allows assessment of the algorithm performance with regard to the diurnal variation that the MODIS validation lacked. GOES sounder retrievals and SURFRAD ground observations were collocated within 0.5° radius of the ground stations with a 15 minutes temporal window. Figure 4-1 shows an example of GOES-East and GOES-West scans over the US CONUS area. The surface LW ERB parameters were estimated from the Sounder's radiance observations and the retrievals. The sounding retrievals are available only for clear sky conditions. Operational GOES 11/12 Sounder retrievals from Jan 4 to Sept 30, 2008 were collocated with the SURFRAD ground observations. Since the GOES sounder can only derive sounding for clear sky condition, clear sky condition is therefore assumed whenever GOES sounding is available.

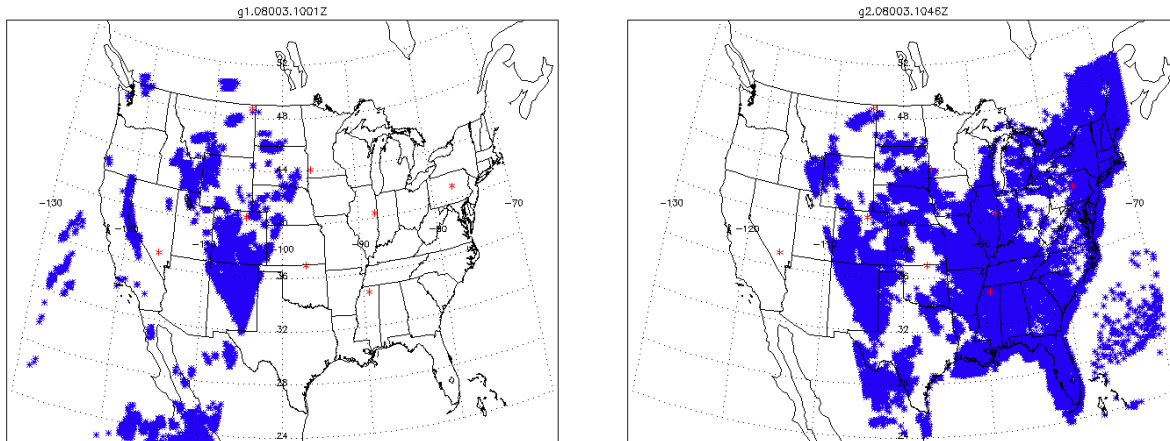


Figure 4-1 Examples of the coverage of GOES Sounding retrievals (blue) related to the ground stations (red) in SURFRAD and ARM networks. Although the GOES Sounders make observations at every 30 minutes interval, the sounding product is only available by hourly.

### Collocation Requirements

The spatial collocation is more stringent for the GOES test to minimize scene-mismatching errors. These are the spatial collocation and temporal homogeneity requirements:

- Distance is less than 0.05 degrees in lat/lon differences between GOES FOV and Ground site
- Standard deviation of ground observed DLR in 15 minutes is less than  $3 \text{ Wm}^{-2}$ .

Spatial and temporal collocation:

- Distance is less than  $0.05^\circ$  between GOES FOV and Ground site
- Ground observations are averaged over a 15-minute interval that encompass the satellite scanning observations.

Temporal and spatial homogeneity tests:

- Standard deviation of ground DLR observations in 15 minutes interval (from five 3-minute averages) needs to be smaller than  $3 \text{ Wm}^{-2}$ .
- Standard deviation of satellite DLR retrievals in  $1^\circ$  circle surround the surface stations needs to be smaller than  $10 \text{ Wm}^{-2}$ .

Empirical cloud contamination removal:

- The cases that have  $\text{netLW} < 30 \text{ Wm}^{-2}$  are considered cloudy sky condition and were removed. This threshold is chosen arbitrarily.

## 4.2 Output from Simulated/Proxy Inputs Data Sets

The LPLA algorithm was implemented using nine months worth of GOES Sounder retrievals to estimate DLR. The inputs for the LPLA are the temperature, total precipitable water, skin temperature, and surface temperature. The GOES-estimated DLR is compared to the Precision Infrared Radiometer (PIR) downwelling thermal flux measurement from seven SURFRAD sites. Figure 4-2 shows the scatter plots of the satellite-estimated DLR from LPLA algorithms, respectively, compared to the SURFRAD ground measurements. The DLR comparison statistics are listed in Tables 4-1. For reference purpose,

Table 4-2 shows the previously established error estimates for LPLA using ARM and BSRN/CMDL ground observations and this shows that the GOES sounder based DLR retrievals have comparable errors.

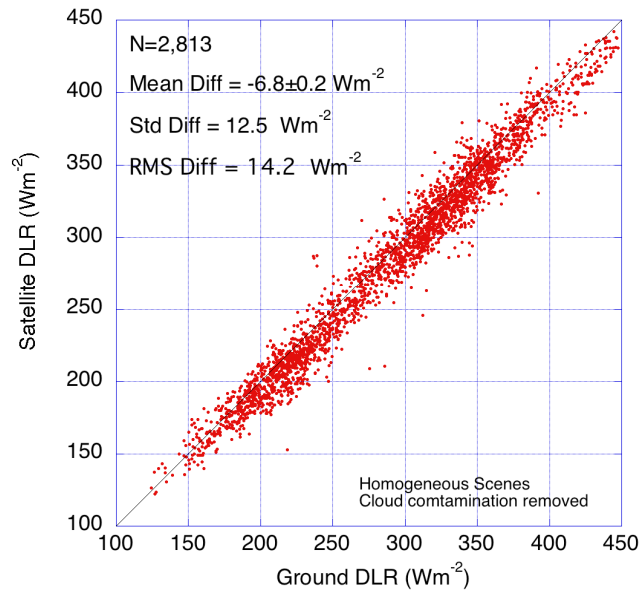


Figure 4-2 Comparison of GOES Sounder-based DLR estimates against SURFRAD observations for homogeneous clear sky scenes.

Table 4-1 DLR comparison statistics. Note that the apparent cloud contaminated cases were eliminated with the empirical filtering on the surface Net LW fluxes.

	Mean (Wm <sup>-2</sup> )	STD (Wm <sup>-2</sup> )	RMS (Wm <sup>-2</sup> )	N
LPLA minus SURFRAD	-6.8±0.2	12.5	14.2	2813

Table 4-2 Error statistics for comparisons between CERES-retrieved and ground measured surface downward LW fluxes.

Clear-Sky LW Flux Statistics			
	# pts.	Bias (Wm <sup>-2</sup> )	RMS (Wm <sup>-2</sup> )
ARM/SGP	2061	-4.6	20.6
BSRN/CMDL	306	-11.9	18.9
All-Sky LW Flux Statistics			
ARM/SGP	4787	-2.1	20.8
BSRN/CMDL	1364	-8.3	18.6

### Empirical Cloud Filtering

Although the GOES sounder only performs retrieval when it is identified as clear sky condition, there are times that could have misidentification and this resulted in large DLR errors in some of the collocated samples. The Net LW is very sensitive to the presence of cloud and we use the ground observed Net LW as a measure to remove the cloudy cases. A threshold of  $30 \text{ Wm}^{-2}$  was set to filter out cloud-contaminated samples. Figure 4-3 shows the relationship of the DLR errors as function of the net LW.

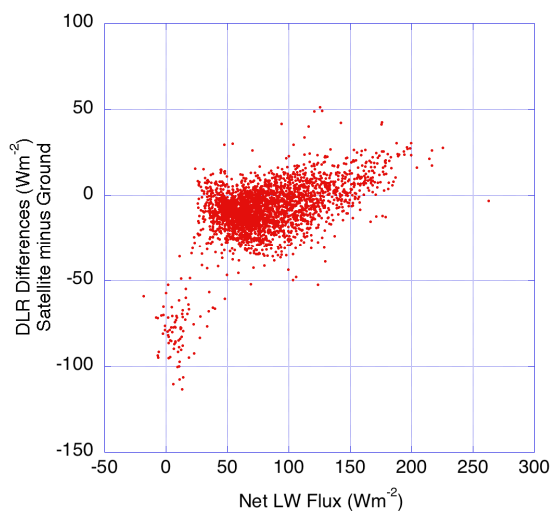


Figure 4-3 DLR errors are shown as a function of the surface net LW where the low net LW values are usually associated with the presence of low clouds.

The match-up data sets seem to contain many cloud contaminated cases that can be easily spotted on the time series plot (Figure 4-4). The downward solar radiation can easily identify the presence of cloud during daytime. The presence of clouds can also be identified with the spiked or strong increase of downward LW fluxes and therefore with relatively smaller net LW fluxes. Although it is possible to remove outliers during the validation study, the scene-misidentification is nevertheless always a possible source of mismatch errors. These cloud-contaminated cases are partially responsible for the overall under-estimation in current results.

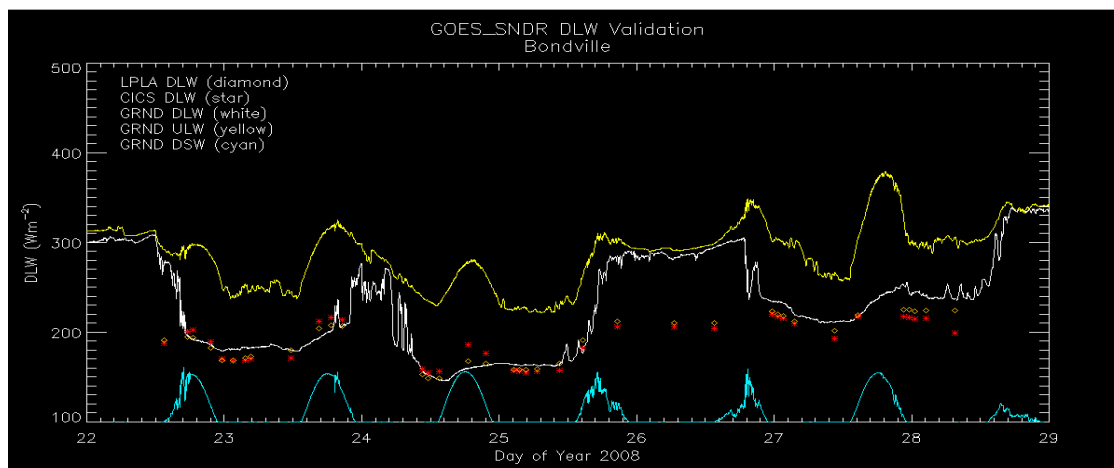


Figure 4-4 Examples of the time series of SURFRAD flux measurements and GOES DLR estimates. LPLA DLR (orange diamond); PIR downwelling thermal radiation (white curve); PIR upwelling thermal radiation (yellow curve); PSP downwelling solar radiation, values scaled by one tenth (cyan curve). The typical errors resulted from misidentification of cloudy conditions as clear were shown in Day 26.

### Local Time Dependence

The diurnal features could be caused by the error characteristics of the sounding retrieval (near surface air temperature, skin temperature and total precipitable water), the satellite algorithms, or in the calibration of ground observations. It is more likely that this is caused by the diurnal errors in satellite sounding retrievals, or the implicit error embedded in the algorithms that relates to the inappropriate estimate of atmospheric emitting temperature for a heated surface during the afternoon period.

Figure 4-5 shows the local time dependent error characteristics in the satellite-derived DLR that appeared to have a positive bias near the noontime.

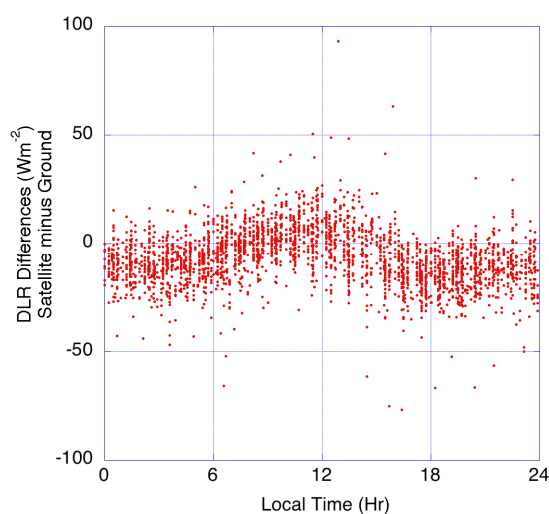


Figure 4-5 Satellite DLR estimation errors are shown as functions of the local time. The DLR estimation seems to have local time-dependent biases when compared to the SURFRAD ground observations.

### Investigation of Error Sources

The possible error sources in DLR retrieval reside in the input parameters as well in the algorithm parameterization. The input parameters include the input parameters: surface temperature, surface pressure, temperature profile, and total precipitable water. The presence of clouds can always mislead the validation results. We use the surface and RAOB observations to assess the DLR errors.

#### Total Precipitable Water (TPW)

To investigate how the satellite retrieved is responsible for the DLR errors, we compared the satellite retrieved PW to that from the RAOB moisture profile. The comparison of PW between GOES retrieval and RAOB showed that the GOES retrieval is in average about 0.11 cm higher than the RAOB. (Figure 4-6)

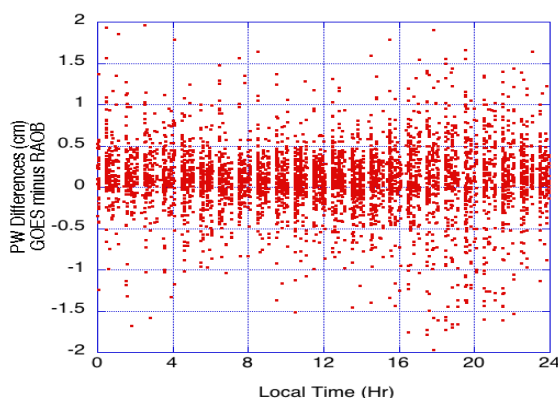


Figure 4-6 Difference of the precipitable water between GOES retrieval and RAOB. GOES total precipitable water for the seven SURFRAD sites has a mean 0.11 cm bias compared to the RAOB. Except with slightly larger degree of spread during later afternoon hours, the PW differences do not seem to have diurnal dependence that could explain the DLR errors.

When using RAOB total precipitable water, the DLR estimate will be lowered in average by about  $5.5 \text{ Wm}^{-2}$ . This resulted in even bigger negative biases in the GOES DLR estimations, thus this cannot explain the overall negative underestimate problems. The PW retrieval errors did not show strong diurnal dependence, either.

#### Cloud contamination

The presence of clouds in the scope of the ground observation usually increases the amount of DLR, causing negative biases in “clear-sky” satellite DLR estimations. This effect is illustrated in Figure 4-7.

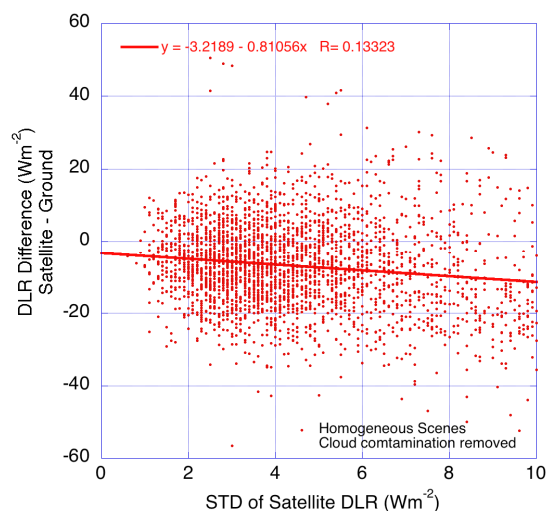


Figure 4-7 DLR differences between satellite retrievals and ground observations are plotted as a function of the standard deviation of the satellite clear sky DLR retrievals within  $0.5^\circ$  radius of the ground stations. The linear fit shows a negative slope, indicating the effects of scene in-homogeneity on the estimation biases.

### In-situ surface temperature

The errors in the input parameters will enter the DLR estimation in various degrees of magnitude. Surface temperature is one of the sensitive parameters (see Figure 4-8). We experiment DLR retrievals with in-situ observations to determine the error properties.

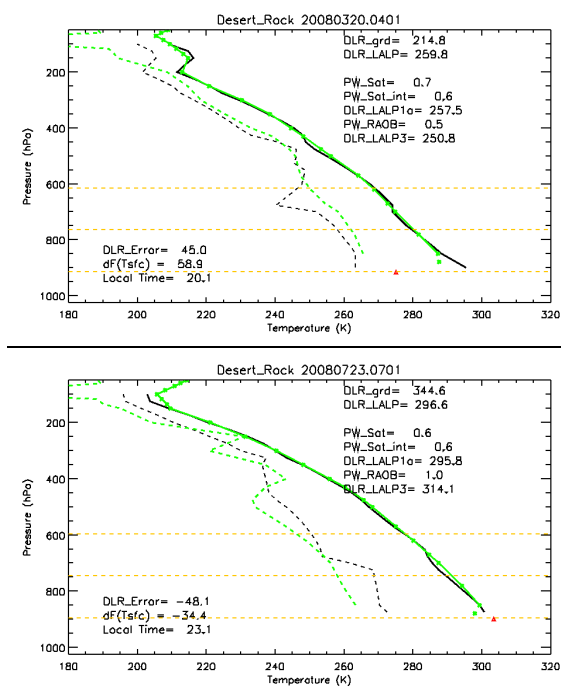


Figure 4-8 Examples of DLR errors in relation with surface temperature retrieval errors in clear sky condition. The red triangle symbol indicate the surface air temperature observed in the 10 m tower at the station, while the green dot indicates the satellite retrieved surface temperature. (Note that the pressure levels of the two symbols can be different that is the error in the surface pressure analysis the satellite retrieval used) A significant portion of the DLR errors can be attributed to the surface temperature errors in these scenarios (see stats at the bottom left corner in each plot).

We use the air temperature measurements on the 10-meter tower at the station to represent the surface temperature. The DLR retrieval using 10-m air temperature to represent surface temperature have significantly improved the accuracy, with a standard deviation of about  $9 \text{ Wm}^{-2}$ , compared to about  $12 \text{ Wm}^{-2}$  when using GOES-retrieved surface temperature (Figure 4-9). And, most importantly, the diurnally dependent DLR retrieval errors previously seen are now disappeared (Figure 4-10). This strongly suggests that the GOES skin temperature retrieval (as part of the sounding product) is the primary error source that causes the diurnally dependent DLR errors in our assessment.

The DLR errors are also shown to be dependent on the total precipitable water. It is not clear at this point whether this is caused by the errors in the moisture profile retrieval or the representativeness errors in the algorithm parameterizations (Figure 4-11). Note that in this experiment, the station reported surface pressure was used.

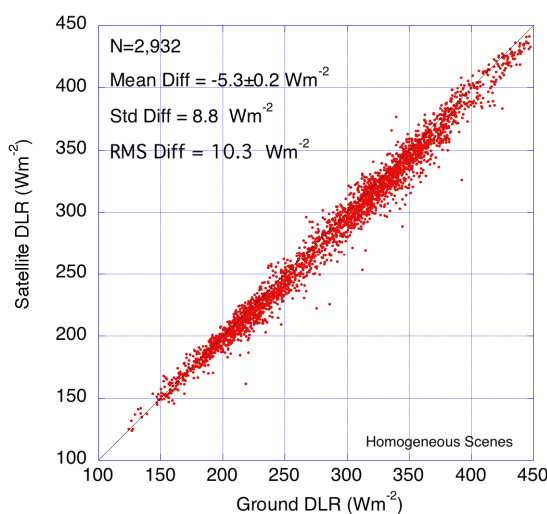


Figure 4-9 Comparison of satellite retrieved DLR versus the ground observations. The satellite DLR retrievals use the 10-m air temperature to represent the surface temperature. It is clearly shown that these DLR retrievals are much more accurate than those using satellite-retrieved surface temperatures.

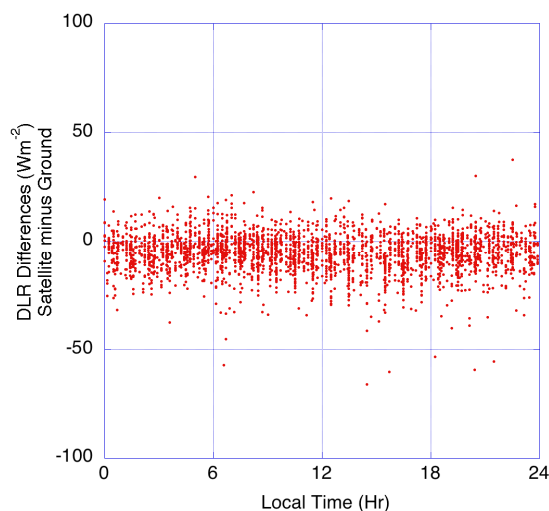


Figure 4-10 Using the 10m air temperature as the surface temperature input for DLR retrieval nearly entirely removed the diurnal dependence of errors that were previously seen. This strongly suggests that the GOES skin temperature retrieval (as part of the Sounding product) has diurnally dependent errors.

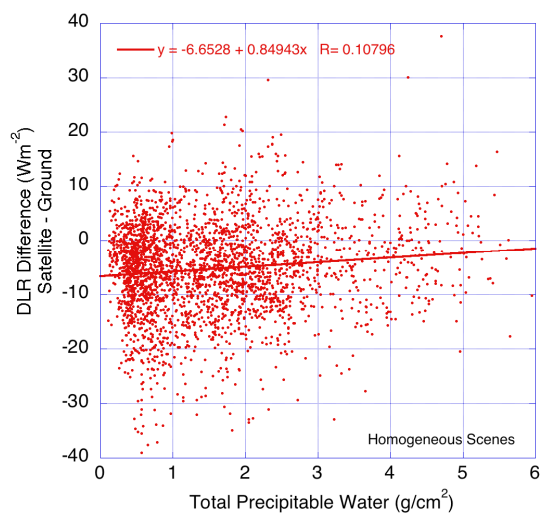


Figure 4-11 This plot suggests that the DLR errors seem to be dependent on the total precipitable water.

### In-situ surface temperature and RAOB temperature/moisture profile

To further pin down the errors in the input parameters, we performed the DLR retrievals using the surface observed 10-meter air temperature and the RAOB temperature and moisture profiles. The SURFRAD data center derived the RAOB profiles interpolated to the stations from the 00Z or 12Z RAOB observations. For this experiment, a 3-hour

window is adopted to temporally collocate RAOB profiles with the SURFRAD observations.

Unexpectedly, the DLR retrieval performances with the RAOB profiles are not as good as using satellite sounding retrievals – with a standard deviation in DLR differences of  $12.4 \text{ Wm}^{-2}$  versus  $8.8 \text{ Wm}^{-2}$  in previous case (Figure 4-12). Note that the number of cases is greatly reduced due to the temporal collocation restriction and this might be responsible for the slightly increased standard deviations. The 3-hour temporal collocation window may also be partially responsible for the increased uncertainties.

The dependence of DLR estimation errors on the total precipitable water is more clearly shown, qualitatively consistent with the in-situ surface temperature experiment (compare Figures 4-11 and 4-13). This requires further study to confirm if this problem is related to the parameterization of the effective atmospheric emissivity.

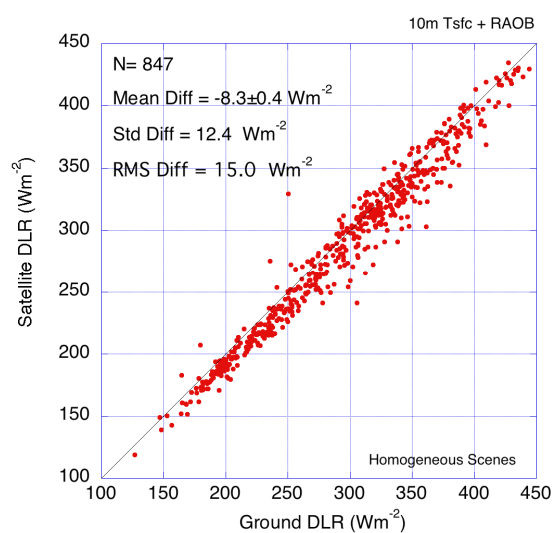


Figure 4-12 Comparison of satellite retrieved DLR versus the ground observations. The satellite DLR retrievals use the 10-m air temperature and RAOB profiles.

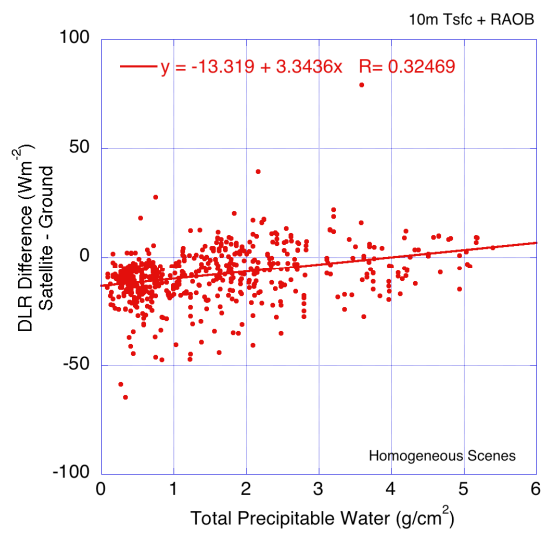


Figure 4-13 DLR errors are shown to be strongly dependent on the total precipitable water, with a correlation of 0.32. This is consistent with the previous experiment that only uses in-situ surface temperature. This seems to suggest representativeness errors in the LPLA algorithm effective emissivity parameterization that we need to pursue further investigations.

#### 4.2.1 Accuracy and Precisions of Estimates

Table 4-3 summarizes the estimated accuracy and precision for the LPLA DLR algorithm assessed with the nine months of GOES sounder data compared to the SURFRAD ground observations. These results indicate that the DLR algorithm meets the F&PS 100% requirements.

Table 4-3 F&PS requirement and the estimated DLR accuracy and precisions.

	F&PS			Algorithm Evaluation		
	Accuracy	Precision	Range	Accuracy	Precision	
Wm <sup>-2</sup>						
<b>DLR</b>	25	20	50-750	7	13	Offline

#### 4.2.2 Error Budget

The LPLA DLR algorithms consider the DLR as the downward emission from the atmosphere as a grey body that reaches the earth surface. The effective emitting temperature and a corresponding effective emissivity are parameterized with near surface temperatures and total precipitable water.

Assuming an emitting temperature of 288°K at emissivity of one, the DLR error rate due to the error in emitting temperature is about  $5.4 \text{ Wm}^{-2}\text{K}^{-1}$ . A 1% error in emissivity will lead to about a 3.9  $\text{Wm}^{-2}$  DLR error. On average, 1 mm error in the total precipitable water could introduce about 5  $\text{Wm}^{-2}$  errors in the DLR for LPLA parameterization.

### Unit Test Readiness Results

The development and tests are performed on orbit199l.orbit2.nesdis.noaa.gov – Linux (2.33GHz 2 dual core CPUs with 2 GB memory/CPU, 2TB disk space). The machine is physically located at NOAA/NESDIS/STAR within the STAR collaborative environment and maintained by STAR IT.

A sample data set containing 1000 cases has been used in the Framework Software Readiness Test. The input variables include surface temperature and pressure and their vertical profiles, and the total precipitable water. The reference DLR flux data provided is derived from the offline system at CICS. The resulting DLR flux values are exactly the same as the offline results – Zero pixels differ.

## **5 PRACTICAL CONSIDERATIONS**

### **5.1 Numerical Computation Considerations**

DLR retrieval is performed on the pixel basis, independent of other pixels. This is ideal for vector processing. Although the flow chart is now designed for pixel processing, it would be more efficient to extend it to one scan unit, or the next larger processing unit, e.g., a granule.

### **5.2 Programming and Procedural Considerations**

The DLR is a pixel-by-pixel algorithm. The LPLA clear sky DLR algorithms require ancillary inputs including temperature, total precipitable water, surface temperature and surface pressure. The DLR is part of the Earth radiation budget production modules and should be located near the end of the ABI production chain.

The ABI Sounding product is generated at a target of 5x5 pixels. The Sounding products will be sub-sampled to the underlying grids to provide input to DLR calculation on the pixel basis.

The required surface temperature input is obtained from AWG retrievals of land skin temperature (LST) or sea surface temperature (SST), in priority order. When neither product is available, an estimated surface temperature is used (see Section 6.1.1 Graceful Degradation).

### **5.3 Quality Assessment and Diagnostics**

The following procedures are recommended for diagnosing the performance of the DLR.

- SURFRAD (near real time)

- ARM (near real time)
- Routine/Operational Product Evaluation and Monitoring are necessary.
- Automatic analysis/statistics generated for collocated ABI and reference sources, including:
  - CERES SARB (not available in real time)
  - NWP surface analysis (LDAS and SST)
  - QA Metrics/Flags to be defined.

#### **5.4 Exception Handling**

The DLR module will check validity of the ancillary input data if flags were provided. The valid range of DLR will also be checked. The missing value will be assigned when calculation results are outside the allowed range.

#### **5.5 Algorithm Validation**

The validation reference data source are from the ground observation networks, including the NOAA Surface Radiation network (SURFRAD) and the DOE Atmospheric Radiation Measurement (ARM) network. These ground stations provide downward longwave radiative flux measurement at a very high frequency and typically 3 minutes average data is used for our validation purpose. The satellite estimated DLR were compared to the concurrent ground observations at certain collocation requirement to yield proper representations of the product accuracy, considering the spatial differences of these two observing methods. As the product is clear sky only, and while cloud contamination can introduce large errors, the effectiveness of cloud filtering is very important to the representativeness of the validation results.

## **6 ASSUMPTIONS AND LIMITATIONS**

The following sections describe the current limitations and assumptions in the current version of the DLR.

### **6.1 Performance**

The ABI DLR algorithms were mainly evaluated using surrogate algorithms tested with the GOES Sounder data. The evaluation was also conducted with smaller amount of MODIS observations (results not shown here). When available, the evaluation of ABI DLR algorithm with the simulated ABI radiance/products will provide more representative performance assessment.

The performance assessment of LPLA DLR retrieval algorithm suggests that this algorithm could meet the F&PS requirements, with given quality of the sounding product. Further improvements in assessment can be made with more rigorous cloud filtering. The diurnal dependence in DLR errors is not fully understood yet.

#### **6.1.1 Graceful Degradation**

The DLR algorithm uses the surface temperature and the lowest 300 hPa temperature information to estimate effective emitting temperature. The input for surface temperature

is obtained from, in priority, ABI land skin temperature (LST) and ABI sea surface temperature (SST) retrievals. There are cases that either no retrieval is produced, e.g., in the coastal zone, or, retrieval is failed. In those cases, extrapolated surface temperatures are used. The surface temperature is estimated by extrapolating the temperatures of the lowest two atmospheric levels to the surface linearly in height. Corresponding degradation QC flag will be set accordingly.

## **6.2 Assumed Sensor Performance**

The DLR derivation involves sounding retrieval products. The effects of sensor biases/noises on DLR retrieval quality cannot be directly estimated.

## **6.3 Pre-Planned Product Improvements**

The overall performance of the ABI DLR algorithm is satisfactory. However, there remains the diurnal dependent errors and overall under-estimation. These are attributed to the intrinsic algorithm deficiencies as well the input data errors. The DLR diurnal-dependent error requires extensive investigations for a fuller understanding.

### **6.3.1 Improvement 1**

Implement lapse rate threshold to overcome over-estimation for super heated surface, e.g., desert or rock. This will improve the robustness of the effective atmospheric emitting temperature estimation. Ultimately, the weighting for the boundary layer temperatures need to be opacity-dependent (or, water vapor dependent) such that it can predict more accurately the effective emitting temperature.

### **6.3.2 Improvement 2**

Collaborate with Sounding team to investigate possible diurnal errors for near surface temperature and water vapor estimations.

### **6.3.3 Improvement 3**

Perform validation using ABI simulation data and sounding retrieval product. This is a necessary step to separate input-related errors from that of the DLR algorithm since the ad hoc algorithm adjustments for surrogate system may not be valid for the ABI.

### **6.3.4 Improvement 4**

Cloudy sky DLR can be generated when cloud amount and cloud base information is available. At the moment, the cloud base is not an ABI product. Cloud base estimation method can be employed to derive cloudy sky DLR.

## **7 REFERENCES**

Darnell, W. L., S. K. Gupta, and W. Frank Staylor, 1983: Downward longwave radiation at the surface from satellite measurements. *J. Climate Appl. Meteor.*, **22**, 1956-1960.

- Ellingson, R. G., 1982: On the effects of cumulus dimensions on longwave irradiance and heating rate calculations. *J. Atmos. Sci.*, **39**, 886-896.
- Ellingson, R. G. and J. C. Gille, 1978: An infrared radiative transfer model, part I: Model description and comparison of observations with calculations. *J. Atmos. Sci.*, **35**, 523-545.
- Ellingson, R. G., D. J. Yanuk, H.-T. Lee, and A. Gruber, 1989: A technique for estimating outgoing longwave radiation from HIRS radiance observations. *J. Atmos. and Ocean. Tech.*, **6**, 706-711.
- Ellingson, R. G., 1995: Surface longwave fluxes from satellite observations: A critical review. *Remote Sens. Environ.*, **51**, 89-97.
- Gupta, S. K., 1989: A parameterization of longwave radiation from sun-synchronous satellite data. *J. Climate*, **2**, 305-320.
- Gupta, S. K., D. P. Kratz, P. W. Stackhouse Jr., A. C. Wilber, T. Zhang, and V. E. Sothcott, 2010: Improvement of Surface Longwave Flux Algorithms Used in CERES Processing. *J. Appl. Meteor. & Clim.* (doi: 10.1175/2010JAMC2463.1) (in print)
- Lee, H.-T. and R. G. Ellingson, 2002: Development of a statistical method of estimating the downward longwave radiation at the surface from satellite observations. *J. Atmos. Ocean. Tech.*, **19**, 1500-1515.
- Warner, J. X. and R. G. Ellingson, 2000: A new narrowband radiation model for water vapor absorption. *J. Atmos. Sci.*, **57**, 1481-1496.

## Appendix 1: Common Ancillary Data Sets

### 1. MDS\_L2\_TPW\_5KM\_FILE

#### a. *Data description*

**Description:** MODIS L2 TPW 5km

**Filename:**

MOD07\_L2.AYYYYYDDD.HHMM.005.yyyydddhhmmss.nc /  
MYD07\_L2.AYYYYYDDD.HHMM.005.yyyydddhhmmss.nc.

Where,

MOD07\_L2/ MYD07\_L2 – Level  
2 Product Name from TERRA (MOD) /  
AQUA (MYD)

A – Nothing to do here

YYYYYDDD – 4 digit year plus 3 digit of Julian day

HHMM – 2 digit of hour and 2 digit of minutes in GMT

005 – Processing system version

yyydddhhmmss – processing date/time

**Origin:** NASA DAAC

**Size:** 31 MB

**Static/Dynamic:** Dynamic

#### b. *Interpolation description*

The closest point is used for each satellite pixel:

In Latitude / Longitude space, use the ancillary data closest to the satellite pixel.

### 2. NWP\_GFS

#### a. *Data description*

**Description:** NCEP GFS model data in grib format – 1 x 1 degree  
(360x181), 26 levels

**Filename:** gfs.tHHz.pgrbfhh

Where,

HH – Forecast time in hour: 00, 06, 12, 18

hh – Previous hours used to make forecast: 00, 03, 06, 09

**Origin:** NCEP

**Size:** 26MB

**Static/Dynamic:** Dynamic

***b. Interpolation description***

There are three interpolations are installed:

**NWP forecast interpolation from different forecast time:**

Load two NWP grib files which are for two different forecast time and interpolate to the satellite time using linear interpolation with time difference.

Suppose:

T1, T2 are NWP forecast time, T is satellite observation time, and  $T1 < T < T2$ . Y is any NWP field. Then field Y at satellite observation time T is:

$$Y(T) = Y(T1) * W(T1) + Y(T2) * W(T2)$$

Where W is weight and

$$W(T1) = 1 - (T-T1) / (T2-T1)$$

$$W(T2) = (T-T1) / (T2-T1)$$

**NWP forecast spatial interpolation from NWP forecast grid points. This interpolation generates the NWP forecast for the satellite pixel from the NWP forecast grid dataset.**

The closest point is used for each satellite pixel:

- 1) Given NWP forecast grid of large size than satellite grid
- 2) In Latitude / Longitude space, use the ancillary data closest to the satellite pixel.

**NWP forecast profile vertical interpolation**

Interpolate NWP GFS profile from 26 pressure levels to 101 pressure levels

For vertical profile interpolation, linear interpolation with Log pressure is used:

Suppose:

y is temperature or water vapor at 26 levels, and y101 is temperature or water vapor at 101 levels. p is any pressure level between p(i) and p(i-1), with p(i-1) < p < p(i). y(i) and y(i-1) are y at pressure level p(i) and p(i-1). Then y101 at pressure p level is:

$$y_{101}(p) = y(i-1) + \log( p[i] / p[i-1] ) * ( y[i] - y[i-1] ) / \log ( p[i] / p[i-1] )$$